arXiv:1702.01372v1 [cond-mat.mtrl-sci] 5 Feb 2017

Topological crystalline antiferromagnetic state in tetragonal FeS

Ningning Hao,[1,*] Fawei Zheng,[2,*] Ping Zhang,[2,3,†] and Shun-Qing Shen[4,‡]

[1]*High Magnetic Field Laboratory, Chinese Academy of Sciences, Hefei, Anhui 230031, China*
[2]*Institute of Applied Physics and Computational Mathematics, Beijing 100088, China*
[3]*Beijing Computational Science Research Center, Beijing 100193, China*
[4]*Department of Physics, The University of Hong Kong, Pokfulam Road, Hong Kong, China*

Stable magnetic order in materials usually breaks some spatial symmetries such that the electronic structures are strongly reconstructed and present some new features such as Dirac-cone structure. Here, we find that tetragonal FeS is a topological insulator with the pair checker-board antiferromagnetic (PCB-AFM)order, named "topological crystalline antiferromagnetic state", in which, the (010) surface of tetragonal FeS supports non-trivial surface states protected by the product of fractional translation symmetry, mirror symmetry, and time-reversal (TR) symmetry, while other surfaces are topologically trivial due to the glide-plane mirror symmetry breaking. Our finding indicates that the non-trivial topological states could emerge accompanying with some magnetic orders, and the corresponding symmetry breaking provides possible ways to modulate charge and spin transport of surface electrons in these classes of materials.

Spin-orbital coupling (SOC) plays a key role to induce topologically non-trivial states [1, 2]. Recently, a sizable SOC in all main families of iron-based superconductors was directly observed by angle-resolved photoemission spectroscopy (ARPES) [3]. The observations support the possibility of the proposal to realize the topological state in single-layer FeSe film grown on $SrTiO_3$ substrate [4]. More recently, the ARPES and scanning tunneling spectroscopy (STS) measurements showed the evidence to support the topological edge state in single-layer FeSe/$SrTiO_3$ and attributed to the coexistence of checkerboard antiferromagnetic (C-AFM) order [5].

As an isostructure to FeSe, tetragonal FeS has attracted great attention since the superconductivity with transition temperature 4.5K was reported [6]. The parallel studies of tetragonal FeS are of great benefit to understand many debated issues in FeSe. One of important aspects of tetragonal FeS is to identify the possibly magnetic-ordered state which gives rise to superconductivity and the interplay between the magnetism and possibly non-trivial topology. To date, a variety of magnetic states have been proposed for tetragonal FeS experimentally, such as a commensurate antiferromagnetic order below T_N=116 K with wave vector k_m= (0.25, 0.25, 0) from neutron scattering measurement [7], as well as a low-moment (10^{-2}∼10^{-3} μ_B/Fe) magnetic phase (with T_N=20 K) coexisting with superconductivity and the presence of a small non-superconducting magnetic phase with $\sim 1.0\mu_B$/Fe in tetragonal FeS from muon spin rotation measurements [8, 9]. These sample-dependent inconsistencies may need further efforts to be devoted to the high-quality single crystal synthesis and relevant thin film growth.

Theoretically, first-principles calculations provide an effective approach to address the magnetic ground state of tetragonal FeS, whose crystal structure is shown in Fig. 1(a). Here, by adopting the experimental crystalline parameters and taking into account the suitable electron correlated effect, our calculations show that the PCB-AFM state with the pattern of magnetization shown in Fig. 1(c) is the magnetic ground state [10, 11], which is different from previous predictions[12, 13]

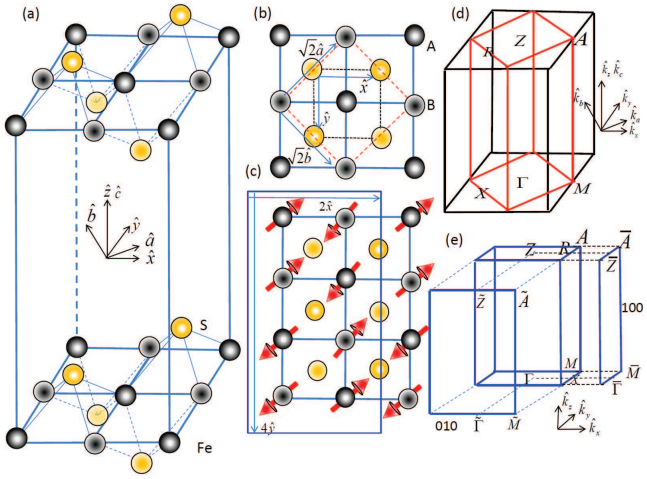

FIG. 1: (Color online)(a) The 3D view of crystal structure of tetragonal FeS. Different filling balls denote different sublattices. (b)-(c) The top-down view of patterns of paramagnetic (PM) and PCB-AFM orders. In (b) the black-dotted and red-dashed lines label the one-Fe and two-Fe unit cells, while in (c) the solid-blue lines label the unit cell of PCB-AFM phase. (d) Bulk Brillouin zones of (a). (e) Middle: bulk Brillouin zone of PCB-AFM phase; Left: (010)-surface Brillouin zone; Right: (100)-surface Brillouin zone. Here, we take one-Fe-unit-cell constant as length scale. $(\hat{x},\hat{y},\hat{z})$, $(\hat{a},\hat{b},\hat{c})$, $(\hat{k}_x,\hat{k}_y,\hat{k}_z)$, $(\hat{k}_a,\hat{k}_b,\hat{k}_c)$ denote the unit direction vectors in lattice and momentum space, respectively.

[See Supplementary Materials (SMs) for details]. In the absence of SOC, we find that the band structure in PCB-AFM state is strongly reconstructed and one of its remarkable features is the emergence of Dirac point in certain k_z plane as shown in Fig. 2(b). Slightly finite electron or hole doping can shift the Fermi level away from the Dirac point, and the Fermi surfaces form two thin tubes in three dimensional momentum space shown in Fig. 2(c). It means the PCB-AFM state belongs to node-line semimetal in undoped case without SOC. In the presence of SOC, the Dirac node lines can

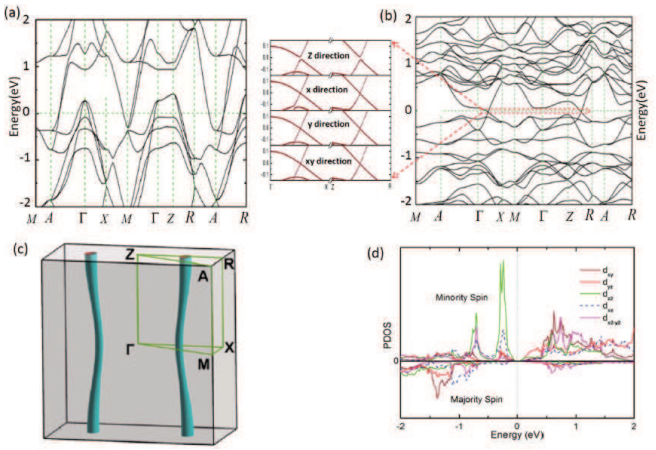

FIG. 2: (a), (b) The band structures for PM and PCB-AFM states in the absence of SOC. The insert in (b) is the zoom-in of the bands in the presence of SOC for the red/dashed rectangle region shown in (b). (c) 3D Fermi surface when the Fermi level is slightly shifted from zero. (d) The partial density of states in the absence of SOC.

open a gap or not depending on the orientation of the magnetic moments as shown in the inset of Fig. 2(b). Namely, the out-of-xy-plane magnetization can break the Dirac node lines and open a gap while the Dirac node lines are robust against the in-xy-plane magnetization. Further calculations show that the gapped PCB-AFM state with out-of-xy-plane magnetization inherits an extraordinary topological state, which we call "topological crystalline antiferromagnetic state". Our symmetry analyses prove that the (010) surface of tetragonal FeS in topological crystalline antiferromagnetic state hosts helical surface states protected by the product of fractional translation symmetry $\frac{1}{2}\hat{t}(2\hat{x},0,0)$, mirror symmetry M_z, and TR symmetry $\hat{T}$, in which $\hat{t}$ denotes the translation operation and $\hat{M}_z$ is the mirror reflection about xy-plane, while other surfaces, such as (100) and (001), are topologically trivial due to the absence of glide-plane mirror symmetry $\frac{1}{2}\hat{t}(0,4\hat{y},0)\hat{M}_z$. In the following, first, we clarify how the band structures evolve from the PM state to PCB-AFM state from the tight-binding analyses associated with the first-principles calculations. Second, we demonstrate and prove the existence of topological crystalline antiferromagnetic state from symmetry analyses associated with the numerical calculations.

To understand the physical picture of the band reconstruction of PCB-AFM state, we start with a tight-binding (TB) Hamiltonian which includes five d orbitals of Fe atom, because the partial density of states in Fig. 2(d) shows that only the d orbital weights are large around the Fermi energy. Our TB Hamiltonian can reproduce the band structure of PM state within the energy window $[-3.0, 3.0]$ eV from the first-principles calculation,

$$H_0 = \sum_{k\in BZ_{pm}} \sum_{\alpha,\beta,\sigma} \Psi^{\dagger}_{\alpha,\sigma}(\mathbf{k}) H_{\alpha\beta}(k) \Psi_{\beta,\sigma}(\mathbf{k}). \quad (1)$$

Here, $\mathbf{k}=(k_x,k_y,k_z)$ is defined in one-Fe unit cell with $(k_x,k_y)\in[0,2\pi]$, $k_z\in[0,2\pi/c]$. We have transformed the TB Hamiltonian from two-Fe-unit-cell representation to one-Fe-unit-cell representation with help of the glide-plane symmetric operator $\frac{1}{2}\hat{t}(\sqrt{2}\hat{a},\sqrt{2}\hat{b},0)\hat{M}_z$. The detailed discussions about the relationship between the one-Fe unit cell and two-Fe unit cell can be found in Ref. [14]. α,β take o or e to label the parity of the glide-plane symmetry. σ labels spin degree of freedom. $\Psi^T_{o,\sigma}(\mathbf{k})=[d_{xy,\sigma}(\mathbf{k}+\mathbf{Q}), d_{x^2-y^2,\sigma}(\mathbf{k}+\mathbf{Q}), d_{xz,\sigma}(\mathbf{k}), d_{yz,\sigma}(\mathbf{k}), d_{z^2,\sigma}(\mathbf{k}+\mathbf{Q})]$ and $\Psi_{e,\sigma}(\mathbf{k})=\Psi_{o,\sigma}(\mathbf{k}+\mathbf{Q})$ with $\mathbf{Q}=(\pi,\pi,0)$ denoting the folding wave vector from one-Fe BZ to two-Fe BZ. $H_{oo}(k)$ and $H_{ee}(k)$ describe the TB Hamiltonian with odd and even parity of glide-plane symmetry. $H_{oe}(k)$ and $H_{eo}(k)$ describe the parity mixing terms. The exact expressions for $H_{\alpha\beta}(k)$ are presented in SMs. The PM band structure from the Hamiltonian in Eq. (1) is shown in Fig. 3(d), which is quite similar to the band structure obtained from the first-principles calculations as shown in Fig. 2(a). In PCB-AFM state, one magnetic unit cell includes eight Fe atoms as shown in Fig. 1(c), and the corresponding folding wave vector is $\mathbf{Q}_1=(\pi,\pi/2,0)$. The folding Hamiltonian describing the band structure of PCB-AFM state is

$$H^{(l)}_{PCB} = \sum_{n=0}^{3} \sum_{k_n\in BZ_{pcb}} \sum_{\alpha,\beta,\sigma} [\Psi^{\dagger}_{\alpha,\sigma}(\mathbf{k}_n) H_{\alpha\beta}(k_n) \Psi_{\beta,\sigma}(\mathbf{k}_n) + \delta_{\alpha\beta}\Psi^{\dagger}_{\alpha}(\mathbf{k}_n)\Delta_{pcb} e^{-i\frac{(n-2\alpha)\pi}{2}} s_l \Psi_{\beta}(\mathbf{k}_{n+1}) + H.c.]. \quad (2)$$

Here, $\mathbf{k}_n=\mathbf{k}+n\mathbf{Q}_1$. s_l span spin space with $l=0,x,y,z$ the 2×2 unit matrix and Pauli matrices, respectively. Δ_{pcb} is the PCB-AFM order parameter with the form of a 5×5 diagonal matrix, namely, $\Delta_{pcb}=\text{diag}[m_{xy}, m_{x^2-y^2}, m_{xz}, m_{yz}, m_{z^2}]$. Note that only the intra-orbital magnetic moments are dominant. Given the PCB-AFM order parameters shown in the caption of Fig. 3, the Hamiltonian in Eq. (2) can reproduce the band structures from the first-principles calculations shown in Fig. 2(b), from which we can find that the Dirac band structure emerges around the Fermi surface.

To elaborate the formation of the Dirac band structure in the absence of SOC, we analyze the band reconstruction from the PM state to PCB-AFM state. Given the selected magnetic BZ with $k_x\in[-\frac{\pi}{2},\frac{\pi}{2}], k_y\in[-\frac{\pi}{4},\frac{\pi}{4}]$, for details and step by step, we plot the band structure of PM state along the high-symmetry line $M-\Gamma-X$ in the magnetic BZ in Fig. 3(c1), and find that the bands 1 and 2 are from the $H_{ee}(\mathbf{k}_2)$ and $H_{oo}(\mathbf{k}_2)$ while the bands 3 and 4 are from $H_{oo}(\mathbf{k}_0)$. After the orbital energy modulations $\Delta\varepsilon$ are tuned on in Fig. 3(c2), the degeneracy between bands 3 and 4 with xz and yz orbital weights at Γ point are broken and only band 3 is still close to Fermi surface. This feature indicates that the nematicity is inevitable, consistent with the absence of C_4 rotation symmetry of PCB-AFM state. When four m except xy orbitals are further tuned on, we obtain the bands shown in Fig. 3(c3), and find that the band 1 mainly has $yz_e(\mathbf{k}_2)$ and $z^2_e(\mathbf{k}_2)$ orbital weights, band 2 mainly has $xy_e(\mathbf{k}_2)$ and $xz_e(\mathbf{k}_2)$ orbital weights, and band 3 mainly has $xy_o(\mathbf{k}_2)$ and $xz_o(\mathbf{k}_2)$ orbital

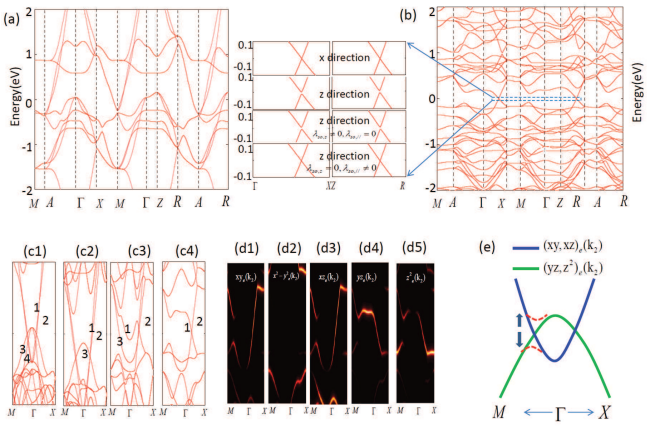

FIG. 3: (a)-(b)The fitting band structures of PM and PCB-AFM states with the Hamiltonian in Eq. (1) and Eq. (2) in the absence of SOC. The insert in (b) is the room-in bands in blue/dasehed rectangle region of (b) in the presence of SOC with $\lambda_{so,z}$=0.03 eV and $\lambda_{so,\parallel}$=0.03 eV. In the case of PCB-AFM state, the modulations of the orbital energy (in unit of eV) about the PM state and the PCB-AFM order parameters (in unit of μ_B) take the magnitudes as follows, $\Delta\varepsilon_{xy}$=−0.1, $\Delta\varepsilon_{x^2-y^2}$=0.2, $\Delta\varepsilon_{xz}$=−0.15, $\Delta\varepsilon_{yz}$=0.15, $\Delta\varepsilon_{z^2}$=0.3; m_{xy}=1.04, $m_{x^2-y^2}$=0.33, m_{xz}=0.25, m_{yz}=0.64, m_{z^2}=0.30. The sum of five m is about 2.5 μ_B as the result obtained from the first-principles calculations. (c1)-(c4) The bands evolution from the PM state to PCB-AFM state along the $M-\Gamma-X$ lines: (c1) shows the bands in PM state, (c2) turn on all $\Delta\varepsilon$ and turn off all m, (c3) turn on all $\Delta\varepsilon$ and turn off only m_{xy}, and (c4) shows the bands in PCB-AFM state. (d1)-(d5) the orbital-resolved spectral function $A_e(\mathbf{k}_2,\omega)$ for five d orbitals. (e) The effective two-band model to capture the Dirac cone structure.

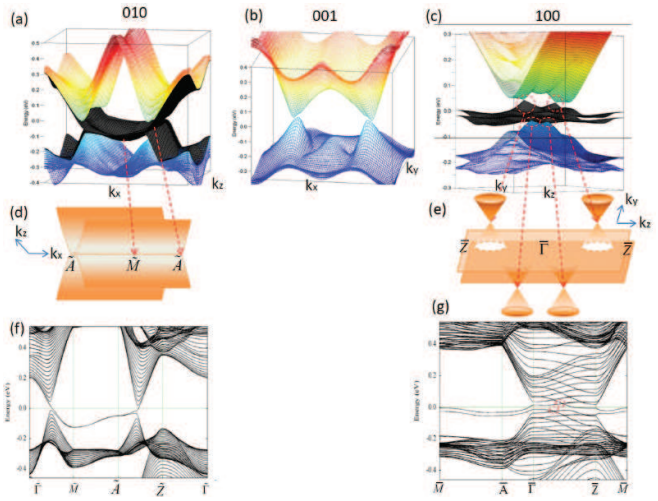

FIG. 4: (Color online)(a)-(c) The band structures of PCB-AFM state with surface cuts about [010], [001], and [100] directions. The thickness of the slab is 20 iron layers in (a), 10 iron layers in (b) and 16 iron layers in (c). The middle black colored bands are localized surface bands. (d) and (e) are schematic diagrams which are topologically equivalent to the local surface bands in (a) and (c). (f) and (g) are the surface bands along the high-symmetry lines of surface BZ shown in Fig. 1(e). The thickness of the slab is 60 iron layers in (f) and 40 iron layers in (g).

weights. Finally, when m_{xy} is further tuned on, the band 3 is heavily pushed up while bands 1 and 2 are slightly modulated, and we obtain the reconstructed band structure of PCB-AFM state shown in Fig. 3(c4). To further support our analysis, we plot the orbital-resolved spectral function $A_\alpha(k_n,\omega)$ in PCB-AFM state in Figs. 3(d1)-(d5). The orbital-resolved weight distribution of spectral function $A_e(k_2,\omega)$ is consistent with the aforementioned analysis. The key features of the Dirac band structures can be extracted and schematically illustrated in Fig. 3(e). The two effective bands mainly have the $(xy,\ xz)_e(\mathbf{k}_2)$ orbital weights for blue colored one and $(yz,\ z^2)_e(\mathbf{k}_2)$ orbital weights for green colored one.

Now, we take into account the SOC contribution to the Hamiltonian, which has the following form,

$$H_{so}=\sum_{n=0}^{3}\sum_{k_n\in BZ_{pcb}}\sum_{\alpha\beta}[\delta_{\alpha\beta}\Psi^\dagger_\alpha(\mathbf{k}_n)\lambda_{so,z}L^z s_z\Psi_\beta(\mathbf{k}_n) + (1-\delta_{\alpha\beta})\Psi^\dagger_\alpha(\mathbf{k}_n)\lambda_{so,\parallel}(L^x s_x+L^y s_y)\Psi_\beta(\mathbf{k}_n)]. \quad (3)$$

Here (L^x,L^y,L^z) are three components of the $L=2$ angular-momentum representation in d-orbital basis, and the explicit forms are shown in SMs. Note that the first term in H_{so} is spin and glide-plane parity conserved, while the second term is spin flipped and glide-plane parity mixed to keep the spatial inversion invariant of H_{so}. The TB band structures in the presence of SOC are shown in the insert part of Fig. 3(b). The TB model gives the consistent results as first-principles calculations shown in the insert of Fig. 2(b). We further clarify that the small gap opening of Dirac point is induced by $\lambda_{so,z}$ but not by $\lambda_{so,\parallel}$ as shown in the third panel in the insert of Fig. 3(b).

In the following, we focus on the the PCB-AFM phase with z-direction magnetization. To reveal the possible non-trivial topology induced by SOC, we perform the first-principles calculation with open boundary conditions for [010], [100], and [001] directions. For tetragonal FeS slab, the energy spectra are shown in Figs. 4(a)-(c) for (010), (001), and (100) S-terminated surface cuts. The results for Fe-terminated surface cuts are similar. We extract the localized surface bands and plot the topologically equivalent schematic diagrams in Figs. 4(d) and 4(e) to show the key features of the surface states. From Figs. 4(d) and 4(e) we can find that the localized (010) surface bands cross the band gap and imply the non-trivial properties, while the middle two localized surface bands of (100) surface are gapped and form Dirac-cone structures with other two bands. To explicate the characteristics of the surface states, we first clarify the symmetries owned by the (010) and (100) surfaces. Given the PCB-AFM pattern shown in Fig. 1(c) and taking the mid-point of Fe-Fe bond as origin, the (010) surface has the glide-plane mirror symmetry $\frac{1}{2}\hat{t}(2\hat{x},0,0)\hat{M}_z$, glideless mirror symmetry $\hat{M}_x$, and glide-

plane TR symmetry $\frac{1}{2}\hat{t}(2\hat{x},0,0)\hat{T}$; the (100) surface has only glide-plane TR symmetry $\frac{1}{2}\hat{t}(0,4\hat{y},0)\hat{T}$. Note that the fractional translation must be combined with point group operators and TR operator to guarantee system invariant under the collaborative operations in the presence of antiferromagnetic order [15]. The surface states can be classified according to the eigen-values of the relevant symmetry. The representations of symmetry operators upon the surface states can be constructed as follows, $\frac{1}{2}\hat{t}(2\hat{x},0,0)\hat{M}_z{=}{-}ie^{-ik_x}s_z$, $\hat{M}_x{=}{-}is_x$, $\frac{1}{2}\hat{t}(2\hat{x},0,0)\hat{T}{=}{-}ie^{-ik_x}s_y\mathcal{K}$, and $\frac{1}{2}\hat{t}(0,4\hat{y},0)\hat{T}{=}{-}ie^{-i2k_y}s_y\mathcal{K}$ with $\mathcal{K}$ the complex conjugate operator.

The topological robustness of the surface states is protected by the symmetries. For details, we first discuss the (010) surface. (1) Along the $\tilde{M}{-}\tilde{A}$ line, the surface bands are a doublet protected by a product operator $\frac{1}{2}\hat{t}(2\hat{x},0,0)\hat{T}\hat{M}_z$, which results in the pseudo-Kramers degeneracy shown in Fig. 4(f) through the anti-unitary property $[\frac{1}{2}\hat{t}(2\hat{x},0,0)\hat{T}\hat{M}_z]^2{=}e^{-i2k_x}|_{k_x=\pi/2}{=}{-}I$. (2) Along both $\tilde{\Gamma}{-}\tilde{M}$ ($k_z{=}0$) and $\tilde{Z}{-}\tilde{A}$ ($k_z{=}\pi$) lines, $[\frac{1}{2}\hat{t}(2\hat{x},0,0)\hat{M}_z]^2{=}{-}e^{-i2k_x}I$ means two branches for mirror eigenvalues: $\pm ie^{-ik_x}$. The TR symmetry enforce the $\frac{1}{2}\hat{t}(2\hat{x},0,0)\hat{M}_z$ eigenvalues to be paired as $\{+i,-i\}$ at $k_x{=}0$ and $\{1,-1\}$ at $k_x{=}\pi/2$. However, the degeneracy points at $\tilde{\Gamma}$ or $\tilde{Z}$ labeled by $\{+i,-i\}$ merge into the bulk bands and no edge states survive along the $\tilde{\Gamma}{-}\tilde{Z}$ line as shown in Fig. 4(f). Fortunately, the degeneracy at $\tilde{M}$ and $\tilde{A}$ points labeled by mirror eigenvalues $\{1,-1\}$ are in the band gap and indicate the non-trivial topological properties of (010) surface states as shown in Fig. 4(f). Note that the degeneracy between $\tilde{M}$ and $\tilde{A}$ can be slightly gapped by artificially adding the symmetry-allowed high-order terms without breaking the degeneracy at $\tilde{M}$ and $\tilde{A}$ points. As such, the node line connected $\tilde{M}$ and $\tilde{A}$ is reduced into two Dirac nodes at $\tilde{M}$ and $\tilde{A}$ points, and the topological nature of (010) surface is characterized by a mirror Chern number $n_M{=}(n_1{-}n_{-1})/2$ [16, 17]. However, the symmetry-allowed high-order terms are negligibly small, because such terms are from the interlayer couplings and correspond to the parity-breaking terms in $H_{o,e}(k)$ in Eq. (2). The constraints from (1) and (2) determine the characteristics of the (010) surface states. For the (100) surface, along $\bar{M}{-}\bar{A}$ line, the product operator has the property, $[\frac{1}{2}\hat{t}(0,4\hat{y},0)\hat{T}]^2{=}{-}e^{-i4k_y}|_{k_y=\pi/4}I{=}I$, thus, the in-gap surface states are not degenerate as shown in Fig. 4(g). Along the $\bar{\Gamma}{-}\bar{Z}$ line, the surface bands cross with other bands to form Dirac-cone structures labeled with the red/dashed circles in Figs. 4(c) and 4(g). The detailed analyses of the features of the surface states are presented in SMs. The remarkable differences between the (010) and (100) surfaces root in the strong nematicity accompanying the PCB-AFM order, which maintains glide-plane mirror symmetry $\frac{1}{2}\hat{t}(2\hat{x},0,0)\hat{M}_z$ of (010) surface, but breaks glide-plane mirror symmetry $\frac{1}{2}\hat{t}(0,4\hat{y},0)\hat{M}_z$ of (100) surface. The further combination between glide-plane mirror symmetry $\frac{1}{2}\hat{t}(2\hat{x},0,0)\hat{M}_z$ and TR symmetry gives the product symmetry $\frac{1}{2}\hat{t}(2\hat{x},0,0)\hat{T}\hat{M}_z$ which protects the topological crystalline antiferromagnetic state here[18]. Besides, the (001) surface is topologically trivial, and can be straightforwardly addressed from Fig. 4(b).

The aforementioned discussions show that the non-trivial surface states inhering in PCB-AFM order in tetragonal FeS are determined by the orientation of magnetization. Thus, modulation of the orientation of magnetization supplies a new method to control the charge and spin transport of the surface states. For the FeS which belongs to a tetragonal crystal, the spontaneous easy axis or easy plane of the magnetization is determined by the intrinsic uniaxial anisotropy and tetragonal anisotropy from the crystallographic structure. Our first-principles calculations show that the energy difference between the case with z-direction magnetization and the case with in-xy-plane magnetization is about 0.25meV/Fe, which is very small, and the recent spin-resolved STM measurements show that the magnetization tends to out-of-xy-plane direction near the surface of bulk $Fe_{1+y}Te$[19]. This indicates that some secondary external effect can play an important role to tune the easy-axis of magnetization, such as pressure, mechanical stresses, and alloying. Indeed, applying mechanical stresses is an effective method and has been widely applied in the study of antiferromagntic state in iron-based superconductors [20, 21]. The strain effect is the "inverse" of magnetostriction, and the energy density associated with the strain can be written as $\mathcal{E}{=}{-}\frac{3}{2}\lambda\sigma\cos^2\theta$, where σ is the stress, λ is the magnetostriction constant, and the angle θ measures the direction of the magnetization relative to the direction of uniform stress. For the positive λ, the easy-axis is z-direction when the stress is along z-direction. Hence, our finding would have substantial implications for transport devices based on new mechanism in spintronics.

In conclusion, we find that an extraordinary topological crystalline antiferromagnetic state inheres in tetragonal FeS with PCB-AFM order, which is protected by the product of fractional translation symmetry, mirror symmetry, and time-reversal symmetry. Our finding sheds light on exploring the new topological phases in materials with magnetic orders, and supplies a complementary route to study the transport behaviors of topological surface states in nanoscale device.

Acknowledgements

This work was supported by NSFC under Grants No. 11674331, No. 11474030, and No. 11625415, by the National Basic Research Program of China under Grant No. 2015CB921103, by 100 Talents Programme of CAS, by the Science Challenge Project under Grant No. JCKY2016212A501, and by President Fund of China Academy of Engineering Physics under Grant No. YZJJLX2016010.

* Equal contribution
† Electronic address: zhang_ping@iapcm.ac.cn
‡ Electronic address: sshen@hku.hk

[1] M. Z. Hasan and C. L. Kane, Colloquium: Topological insulators, Rev. Mod. Phys. **82**, 3045–3067 (2010).

[2] X.-L. Qi and S.-C. Zhang, Topological insulators and superconductors, Rev. Mod. Phys. **83**, 1057 (2011).

[3] S. Borisenko, D. Evtushinsky, I. Morozov, S. Wurmehl, B. Büchner, A. Yaresko, T. Kim, M. Hoesch, T. Wolf, and N. Zhigadlo, Direct observation of spin-orbit coupling in iron-based superconductors, Nat. Phys. **12**, 311-317 (2016).

[4] N. Hao and J. Hu, Topological Phases in the Single-Layer FeSe, Phys. Rev. X **4**, 031053 (2014).

[5] Z. Wang, H. Zhang, D. Liu, C. Liu, C. Tang, C. Song, Y. Zhong, J. Peng, F. Li, C. Nie, L. Wang, X. Zhou, X. Ma, Q. Xue, and F. Liu, Topological edge states in a high-temperature superconductor FeSe/$SrTiO_3$(001) film, Nat. Mat. **15**, 968 (2016).

[6] X. Lai, H. Zhang, Y. Wang, X. Wang, X. Zhang, J. Lin, and F. Huang, Observation of Superconductivity in Tetragonal FeS, J. Am. Chem. Soc. **137**, 10148 (2015).

[7] S. J. Kuhn, M. K. Kidder, W. M. Chance, C. dela Cruz, M. A. McGuire, D. S. Parker, L. Li, L. Debeer-Schmitt, J. Ermentrout, K. Littrell, M. R. Eskildsen, and A. S. Sefat, FeS: Structure and Composition Relations to Superconductivity and Magnetism, arXiv:1603.01598.

[8] S. Holenstein, U. Pachmayr, Z. Guguchia, S. Kamusella, R. Khasanov, A. Amato, C. Baines, H.-H. Klauss, E. Morenzoni, D. Johrendt, and H. Luetkens, Coexistence of low moment magnetism and superconductivity in tetragonal FeS and suppression of T_c under pressure, Phys. Rev. B **93**, 140506 (2016).

[9] F. K. K. Kirschner, F. Lang, C. V. Topping, P. J. Baker, F. L. Pratt, S. E. Wright, D. N. Woodruff, S. J. Clarke, S. J. Blundell, Robustness of superconductivity to competing magnetic phases in tetragonal FeS, arXiv:1607.00953.

[10] H.-Y. Cao, S. Chen, H. Xiang, and X.-G. Gong, Antiferromagnetic ground state with pair-checkerboard order in FeSe, Phys. Rev. B **91**, 020504(R) (2015).

[11] K. Liu, Z.-Y Lu and T. Xiang, Nematic antiferromagnetic states in bulk FeSe, Phys. Rev. B **93**, 205154 (2016).

[12] A. Subedi, L. Zhang, D. J. Singh, and M. H. Du, Density functional study of FeS, FeSe, and FeTe: Electronic structure, magnetism, phonons, and superconductivity, Phys. Rev. B **78**, 134514 (2008).

[13] K. D. Kwon, K. Refson, S. Bone, R. Qiao, W. Yang, Z. Liu, and G. Sposito, Magnetic ordering in tetragonal FeS: Evidence for strong itinerant spin fluctuations, Phys. Rev. B **83**, 064402 (2011).

[14] N. Hao and S.-Q. Shen, Topological superconducting states in monolayer FeSe/$SrTiO_3$, Phys. Rev. B **92**, 165104 (2015).

[15] R. S. K. Mong, A. M. Essin, and J. E. Moore, Antiferromagnetic topological insulators, Phys. Rev. B **81**, 245209 (2010).

[16] J. C. Y. Teo, L. Fu, and C. L. Kane, Surface states and topological invariants in three-dimensional topological insulators: Application to $Bi_{1-x}Sb_x$. Phys. Rev. B **78**, 045426 (2007).

[17] T. H. Hsieh, H. Lin, J. Liu, W. Duan, A. Bansil, and L. Fu, Topological crystalline insulators in the SnTe material class, Nat. Comms. **3**, 982 (2012).

[18] L. Fu, Topological crystalline insulators, Phys. Rev. Lett. **106**, 106802 (2011).

[19] T. Hänke, U. R. Singh, L. Cornils, S. Manna, A. Kamlapure, M. Bremholm, E. M. J. Hedegaard, B. B. Iversen, P. Hofmann, J. Hu, Z. Mao,J. Wiebe and R. Wiesendanger, Reorientation of the diagonal double-stripe spin structure at $Fe_{1+y}Te$ bulk and thin-film surfaces, Nat. Comms. **8**, 13939 (2016).

[20] J.-H. Chu, J. G. Analytis, K. De Greve, P. L. McMahon, Z. Islam, Y. Yamamoto, and I. R. Fisher, In-plane resistivity anisotropy in an underdoped iron arsenide superconductor-Science **329**, 824 (2010).

[21] M. A. Tanatar, E. C. Blomberg, A. Kreyssig, M. G. Kim, N. Ni, A. Thaler, S. L. Budko, P. C. Canfield, A. I. Goldman, I. I. Mazin, and R. Prozorov, Uniaxial-strain mechanical detwinning of $CaFe_2As_2$ and $BaFe_2As_2$ crystals: Optical and transport study, Phys. Rev. B **81**, 184508 (2010).